Experimental and simulated neon spectra in the 10-nm wavelength region from tokamak and reversed field pinch plasmas

M. Mattioli,[1] K. B. Fournier,[2] L. Carraro,[3] C. DeMichelis,[1] P. Monier-Garbet,[1] M. E. Puiatti,[3] F. Sattin,[3] P. Scarin,[3] and M. Valisa[3]

[1]*Association Euratom–CEA sur la Fusion, Département de Recherches sur la Fusion Contrôlée, Centre d' Etudes de Cadarache, F-13108 St. Paul-lez-Durance Cedex, France*

[2]*Lawrence Livermore National Laboratory, P.O. Box 808, L-41 Livermore, California 94550*

[3]*Consorzio RFX, Corso Stati Uniti 4, I-35127 Padova, Italy*

(Received 8 April 1999)

Experimental neon spectra (in the 10-nm region), from the tokamak Tore Supra and the reversed field pinch experiment RFX, have been simulated. The spectra include lines from three neon ionization states, namely Ne^{7+}, Ne^{6+}, and Ne^{5+} ions. Collisional radiative models have been built for these three Ne ions, considering electron collisional excitation and radiative decay as populating processes of the excited states. These models give photon emission coefficients for the emitted lines at electron density and temperature values corresponding to the experimental situations. Impurity modelling is performed using a one-dimensional impurity transport code, calculating the steady-state radial distribution of the Ne ions. The Ne line brightnesses are evaluated in a post-process subroutine and simulated spectra are obtained. The parts of the spectra corresponding to a single ionization state do not depend on the experimental conditions and show good agreement with the simulated single ionization state spectra. On the other hand, the superposition of the three spectra depends on the experimental conditions, as a consequence of the fact that the ion charge distribution depends not only on the radial profiles of the electron density and temperature, but also of the impurity transport coefficients. Simulations of the Ne spectra (including transport) give confidence in the atomic physics calculations; moreover, they allow the determination of the transport coefficients in the plasma region emitting the considered ionization states. [S1063-651X(99)14510-0]

PACS number(s): 52.55.Ez, 52.55.Fa, 32.30.Rj

I. INTRODUCTION

Gaseous impurity injection is frequently used in tokamak devices to obtain plasmas with large radiation losses (''radiative layer'' scenarios). In these devices, the input energy is absorbed in the plasma center, flows radially to the plasma border and is then deposited on the limiters, i.e., on toroidally and/or poloidally localized surfaces defining the last closed magnetic surface (LCMS). With increasing input power, the limiter heating can become too large and the induced plasma pollution becomes intolerable. The purpose of the gas injection (neon being the most frequently used element) is to produce a toroidally and poloidally uniform peripheral radiative mantle, having as a consequence a uniform deposition of the input energy on the walls and therefore reduced thermal loads and plasma pollution. The problem in these experiments is to obtain the maximum radiated energy while, at the same time, minimizing the supplementary central plasma pollution, due to the impurity injection itself. Smearing out the plasma energy with gaseous injection is useful also in devices equipped with divertors, since the divertor plate heating is always localized. The interest of these gas scenarios has been increased by the fact that the plasma performances improve when the high density limit is approached; indeed, a new regime [the radiative improved (RI) mode], with increased energy confinement time, has been found in the Textor tokamak, and subsequently confirmed in other tokamaks [1].

In these recent neon injection experiments, no extensive spectroscopic emission study has been reported. However, spectroscopic measurements were reported by Huang *et al.* [2] in the Text tokamak; a few $n=2-n=3$ line intensity ratios for Ne VII (n being the principal quantum number) were measured in an experiment devoted to a spectroscopic study of O, F, and Ne Be-like ion emission. In the ''radiative layer'' experiments, the neon injection is generally monitored by the spectroscopic detection of only one strong peripheral line (e.g., one of the components of the Ne VIII doublet at 77 nm); its global effects are deduced by the increments, following the injection, of the following three signals: the bolometric signal (giving directly the radiated power), the visible bremsstrahlung continuum emission, and the continuum soft x-ray emission (the last two signals are connected with the increased core plasma effective charge Z_{eff}, due to the increased central Ne density). Sometimes, when a neutral beam is available, the central density of the fully stripped Ne ions has been deduced by charge exchange recombination (CXR) spectroscopy, i.e., by the observation of a visible transition (e.g., the $n=11$ to $n=10$ transition at 525 nm of the H-like Ne ions), produced by CXR of the fully stripped ions with the beam neutrals [3].

Quantitative analysis of the impurity doped discharges are generally performed simulating the experimental signals by a one-dimensional (1D) impurity transport code, where poloidal symmetry of the impurity density is supposed. In the case of divertor plasmas (e.g., in Asdex-U [4]), which are poloidally asymmetric, the simulated results are applicable only to the equatorial plane (i.e., in a region where 2D effects can, to some extent, be neglected). A simplified recycling and

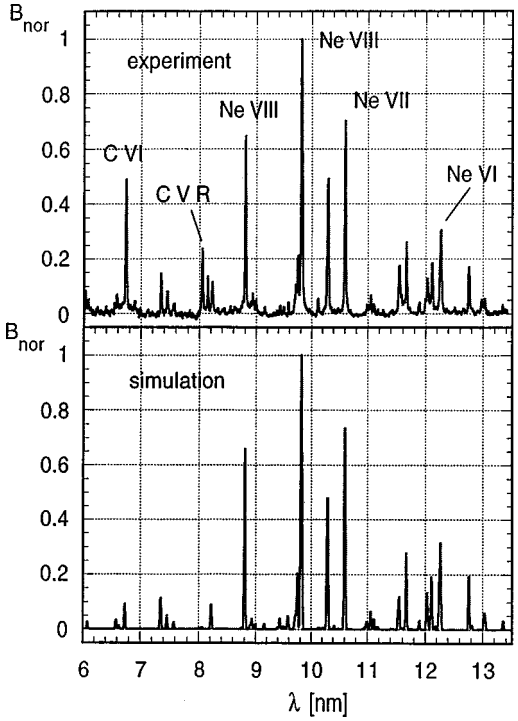

FIG. 1. Experimental (top) and simulated (bottom) neon spectra, between 6.0 and 13.5 nm, from RFX plasmas. The brightnesses B_{nor} are normalized to the strongest 98.2-nm Ne VIII line. The strongest lines are identified (carbon lines are in the second order).

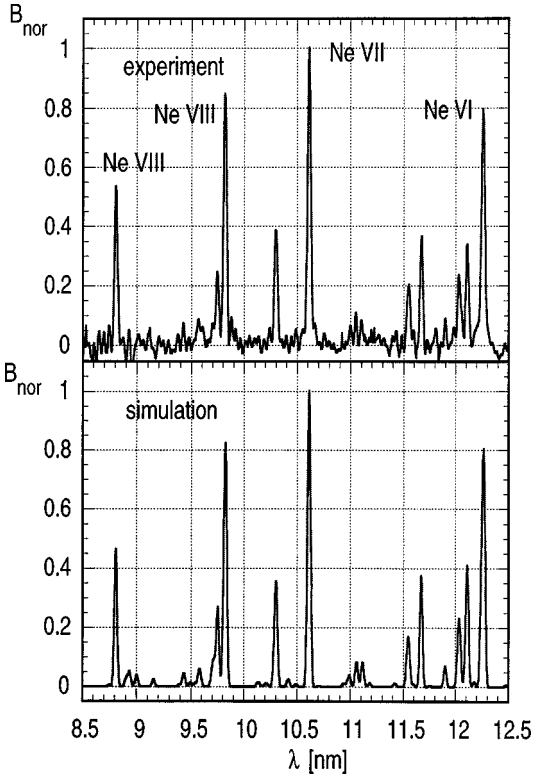

FIG. 2. Experimental (top) and simulated (bottom) spectra between 8.5 and 12.5 nm, from TS plasmas with the ergodic divertor activated. The brightnesses B_{nor} are normalized to the strongest 10.61-nm Ne VII line. The strongest lines are identified.

pumping model is used to achieve a realistic description of the neon source function. Simulations coupling a core plasma impurity transport code with a divertor impurity transport code have also been reported [5], thus taking into account both core and divertor plasma experimental data.

Similar gaseous impurity injection experiments have been performed, for the same reason, in reversed field pinch devices [6]. It must be observed that in these devices the plasma configuration is limited directly by the vessel, and that the toroidal symmetry can be destroyed by interactions associated with the locking in phase of magnetic perturbations that are strongly localized at the wall in a single toroidal cross section.

Experimental Ne emission studies have been reported in the past also for θ-pinch plasmas, e.g., by Lang [7]. Relative brightnesses of both the $n=2-n=2$ and the $n=2-n=3$ Ne VII lines have been interpreted by Lang using collisional radiative (CR) models developed for astrophysical plasmas [8,9]. These CR models have been used to diagnose solar flare plasmas from the experimental observation of line brightness ratios depending either on the electron density n_e or on the electron temperature T_e [10]. Additionally, a few $n=2-n=2$ line ratios of Ne VI have been studied in solar flares [11].

As evident from the discussion above, knowledge of the relevant Ne atomic physics is an essential prerequisite; however, most of the atomic physics data come from theoretical models, with only a few experimental values available. It is one of the main aim of this paper to check the validity of the most recent (and presumably most reliable) atomic physics data calculations for neon, by comparing experimental Ne spectra (in the 10-nm region), obtained in the tokamak Tore Supra (TS) and in the reversed field pinch RFX, with updated simulations. The two devices have been chosen because they have central electron temperatures differing by at least one order of magnitude (but similar electron densities). As far as the electron density is concerned, our observations are unique in that they are in the high density end of the transition region between solar and θ-pinch spectra. Both devices are presented in Sec. II, along with examples of experimental spectra. These include lines from Ne^{7+}, Ne^{6+}, and Ne^{5+} ions, i.e., lines emitted from neon ions of the Li-like, Be-like, and B-like isoelectronic sequences. CR models have been built for these three Ne ions, considering electron collisional excitation and radiative decay as the populating processes of the excited states. Photon emission coefficients (P_{EC}) are given for the lines emitted by the excited levels for n_e and T_e values corresponding to the experimental situations. The CR models are discussed in Sec. III, where, in particular, the included levels and atomic physics data are discussed. P_{EC} and electron collision excitation rate coefficients Q_{exc} are compared with previously reported values. Impurity modeling, briefly described in Sec. IV, is performed with a 1D impurity transport code, calculating the steady-state radial distribution of the Ne ions. The Ne line brightnesses are evaluated in a post-process subroutine and simulated spectra are obtained. It will be shown in Sec. V that the parts of the spectra corresponding to a single ionization state do not depend on the experimental (transport) conditions: each CR model can, therefore, be studied individually and its validity established. On the other hand, the relative amplitudes of the three ''independent'' spectra depend on the ex-

TABLE I. Ne VII collisional excitation rate coefficients computed at 82 eV by CROSS and by using published effective collision strengths [23,24,25]. The levels are indicated by their position in the energy level hierarchy: 1-$2s^2\ ^1S_0$; 2,3,4-$2s2p\ ^3P_{0,1,2}$; 5-$2s2p\ ^1P_1$; 11-$2s3s\ ^3S_1$; 12-$2s3s\ ^1S_0$; 17,18,19–$2s3d\ ^3D_{1,2,3}$; 20-$2s3d\ ^1D_2$; and 21,22,23-$2p3s\ ^3P_{0,1,2}$. The percentage difference between CROSS and the other calculations is also shown. Numbers in square brackets indicate powers of ten.

Transition	CROSS	Ramsbottom [23]	Berrington [24, 25]	Percent difference
1–2	7.64[−11]	1.21[−10]	9.80[−11]	−36/−22
1–3	1.24[−10]	3.64[−10]	2.94[−10]	−66/−58
1–4	3.80[−10]	6.05[−10]	4.89[−10]	−37/−22
1–5	1.54[−8]	1.47[−8]	1.52[−8]	+4/+1
2–11	3.30[−11]	4.82[−11]		−31
3–11	3.40[−11]	4.83[−11]		−30
4–11	3.36[−11]	4.83[−11]		−30
2–17	6.25[−10]	5.23[−10]		+20
2–18	2.39[−11]	3.46[−11]		−30
3–18	4.86[−10]	4.07[−10]		+20
3–19	3.17[−11]	3.98[−11]		−20
4–17	1.93[−11]	2.19[−11]		−12
5–12	2.06[−11]	3.59[−11]		−43
5–20	7.55[−10]	6.33[−10]		+19
Σ(2,3,4)–Σ(21,22,23)	9.1[−11]	9.6[−11]		−5

perimental conditions, as a consequence of the fact that the ion charge distribution depends not only on the radial profiles of n_e and T_e, but also on the radial profiles of the impurity transport coefficients (namely, diffusion coefficient D and inward convection velocity V). As usual in this type of study, the final choice of transport coefficients is not unique; we have constrained it using results of previous transport simulations of intrinsic (carbon and oxygen) impurities in both devices. Finally, concluding remarks are given in Sec. VI.

II. EXPERIMENTAL DATA

A. Neon spectra from the reversed field pinch RFX

RFX is a large reversed field pinch (minor radius $a=0.46$ m, major radius $R=2.0$ m) designed to operate with a plasma current I_p up to 2 MA (currently operated with $I_p=0.5-1$ MA). The central toroidal magnetic field is 0.5–1 T, and no additional heating system is installed. The inconel vacuum vessel is almost completely covered with carbon tiles; carbon and oxygen are, therefore, the main impurities, metals being reduced to very low levels. The impurity content is obtained, as a post-process of the 1D impurity transport code, by coupling absolutely calibrated visible bremsstrahlung emission (at wavelengths around 523.8 and 679.0 nm), soft x-ray data, and XUV spectroscopy [12].

The $n_e(r)$ and $T_e(r)$ profiles, needed as input data for the impurity transport code, are obtained, respectively, by a multichord CO_2 laser interferometer and by a Thomson scattering system coupled with a Si-Li x-ray detector [12,13].

The extreme grazing incidence vacuum spectrometer is equipped with two microchannel plate detectors and has a central line of sight [14]. In the 10-nm region, the spectral range covered by one detector is ~4 nm, with a spectral resolution (full width at half maximum) of ~0.02 nm. It has been possible to extend the spectral range by superposing spectra from similar discharges. The experimental Ne spectra have been obtained with a detector integration time of 20 ms. The instrumental response at different wavelengths has been relatively calibrated against an x-ray source at the $K\alpha$ lines of C, N, C, B, and Be. Additionally, the pixel sensitivity calibration (independent of wavelength) has been measured by varying the position of the spectrum along the multichannel plate detector, and controlling the ratio of a few lines emitted by the same ionization state.

TABLE II. The Li-like configurations used in the model, giving rise to the 76 Ne VIII levels considered.

Li-Like Ne ions (76 levels)	
$1s^22s$	$1s2s^2$
$1s^22p$	$1s2s2p$
$1s^23s$	$1s2s3s$
	$1s2s3p$
$1s^23p$	
	$1s2s3d$
$1s^23d$	
	$1s2s4s$
$1s^24s$	$1s2s4p$
$1s^24p$	$1s2s4d$
$1s^24d$	$1s2s4f$
$1s^24f$	
$1s^25s$	
$1s^25p$	
$1s^25d$	
$1s^25f$	
$1s^25g$	

Figure 1 (top) shows a Ne spectrum between 6.0 and 13.5 nm for a plasma with $n_e(0)=4\times10^{19}\,\mathrm{m}^{-3}$ and $T_e(0)=210$ eV. This spectrum is the superposition of four spectra obtained in similar discharges by displacing the detector carriage. In addition to the injected Ne lines, intrinsic C lines are also clearly visible. They are the second and third order of the C VI Lyman-α (Lyα) line, at 6.74 and 10.21 nm, respectively, and the second order of the resonance and intercombination (R and I) C V lines, at 8.054 and 8.146 nm, respectively. Two line intensity ratios have an atomic physics interest: the I to R ratio (called the G ratio), having a value 0.5—0.6 in these plasma conditions, and the ratio C VI Lyα/C V R, with a value of the order of 1.7–2. Expected oxygen O VI lines (at 11.58 and 12.98 nm) are in this spectrum near the background level.

B. Neon spectra from the TS tokamak

TS is a circular cross section tokamak with supraconducting toroidal magnetic coils. It has a major radius $R=2.25-2.4$ m and a minor limiter radius $a_L=0.7-0.8$ m, with a maximum plasma current of $I_p=2$ MA and toroidal magnetic field of $B_t=4.2$ T. All the exposed surfaces within the vacuum vessel are covered by carbon tiles. It is possible

TABLE III. The Be-like configurations used in the model, giving rise to the 116 Ne VII levels considered.

Be-like Ne ions (116 levels)	
$1s^2 2s^2$	$1s^2 2p^2$
$1s^2 2s2p$	$1s^2 2p3s$
$1s^2 2s3s$	$1s^2 2p3p$
$1s^2 2s3p$	$1s^2 2p3d$
$1s^2 2s3d$	$1s^2 2p4s$
$1s^2 2s4s$	$1s^2 2p4p$
$1s^2 2s4p$	$1s^2 2p4d$
$1s^2 2s4d$	$1s^2 2p4f$
$1s^2 2s4f$	
$1s^2 2s5s$	
$1s^2 2s5p$	
$1s^2 2s5d$	
$1s^2 2s5f$	
$1s^2 2s5g$	

to activate an ergodic divertor (ED), destroying the magnetic surfaces in the edge plasma with a weak resonant magnetic perturbation.

The $n_e(r)$ profiles are obtained by adjusting the spatially resolved vertical Thomson scattering data to the five vertical infrared interferometer channels, with the addition of peripheral data from microwave reflectometry. $T_e(r)$ profiles come from Thomson scattering and electron cyclotron emission data.

Before the neon injection, the impurity content is largely dominated by carbon and oxygen, with negligible amounts of metals (mainly iron or copper). The impurity content is again obtained, as a post-process of the 1D impurity transport code, by coupling absolutely calibrated visible bremsstrahlung emission (at a wavelength around 523.8 nm), soft x-ray data, and XUV spectroscopy. The TS XUV spectrometer is of the same type as that used on RFX, the line of sight being also here central. A longer integration time of 200 ms was used. The instrument response has been calibrated as described above for RFX.

TABLE IV. The B-like configurations used in the model, giving rise to the 228 Ne VI levels considered.

B-like Ne ions (228 levels)	
$2s^2 2p$	$2p^3$
$2s^2 3s$	$2s2p3s$
$2s^2 3p$	$2s2p3p$
$2s^2 3d$	$2s2p3d$
$2s^2 4s$	$2s2p4s$
$2s^2 4p$	$2s2p4p$
$2s^2 4d$	$2s2p4d$
$2s^2 4f$	$2s2p4f$
$2s^2 5s$	$2s2p5s$
$2s^2 5p$	$2s2p5p$
$2s^2 5d$	$2s2p5d$
$2s^2 5f$	$2s2p5f$
$2s^2 5g$	

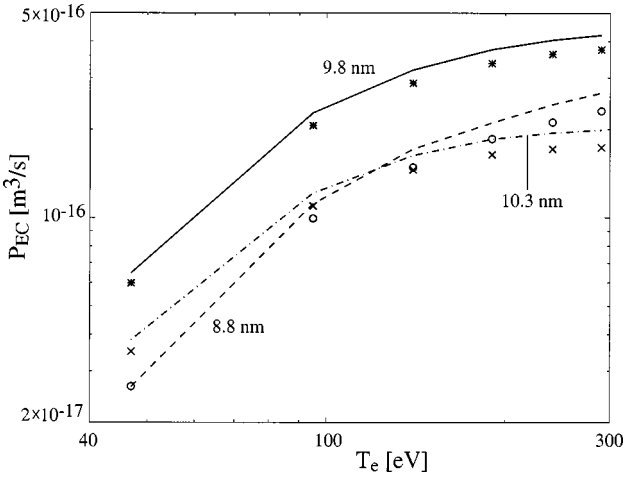

FIG. 3. Photon emission coefficients (P_{EC}, photons $\mathrm{m^3\,s^{-1}}$) as functions of T_e for the following Ne VIII lines: 8.81 nm (dashed line, ○), 9.82 nm (solid line,*), and 10.3 nm (dot-dashed line, ×). Lines are from the present work, and symbols are from Cochrane and McWhirter [28].

Figure 2 (top) shows a Ne spectrum between 8.5 and 12.5 nm. It has been obtained in an ohmic plasma with the ED activated, the main plasma parameters being: $I_p = 1.2\,\mathrm{MA}$, $B_t = 3.3\,\mathrm{T}$, $n_e(0) = 4.5\times10^{19}\,\mathrm{m^{-3}}$, $T_e(0) = 1.7\,\mathrm{keV}$. No intrinsic impurity line is above the background level in this spectrum.

III. ATOMIC STRUCTURE CALCULATIONS AND COLLISIONAL-RADIATIVE MODELS

We describe in this section how the (steady-state) collisional-radiative (CR) photon emission coefficients (P_{EC}) have been computed for Li-, Be-, and B-like neon ions (i.e., respectively, Ne^{7+}, Ne^{6+}, and Ne^{5+}). Each ion has been treated independently from the others. Ionization and recombination into and out of the ground and excited energy levels of each ion have been ignored. The steady state level populations are found by inverting the full CR rate matrix for each ion. The collisional excitation data of the present work are computed in the distorted-wave approximation (DWA).

The atomic data used in constructing the emission models for each ion in the present work are generated from *ab initio* atomic structure calculations with the Hebrew University Lawrence Livermore Atomic Codes (HULLAC). The atomic structure calculations are performed with the graphical angular momentum coupling code ANGLAR [15] and the fully relativistic parametric potential code RELAC [16–18]. For a given ion, RELAC solves the Dirac equation by varying an analytic ionic potential [18], in order to minimize the average energy of a configuration (or of a set of configurations). Once the zeroth-order wave functions are minimized, the configuration-averaged energy of each configuration (or of the set of configurations) has been found, and RELAC calculates the multiconfiguration, intermediate-coupling energy eigenvalues of the fine-structure levels. Inclusion of higher-order energy corrections (Lamb shift, Breit interaction, etc.) is discussed elsewhere [19]. Radiative transition rates are then computed for any requested multipole operator according to the formalism in [20]. The transition rate calculation by RELAC is carried out in the Coulomb gauge (thus in the

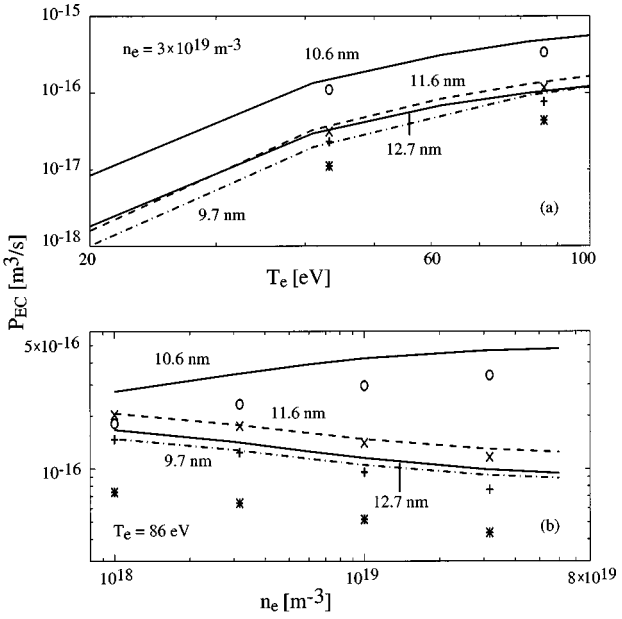

FIG. 4. Photon emission coefficients (P_{EC}, photons $\mathrm{m}^3\,\mathrm{s}^{-1}$) as functions of T_e (top, for $n_e=3\times10^{19}\,\mathrm{m}^{-3}$) and of n_e (bottom, for $T_e=86$ eV), for the following Ne VII lines: 9.75 nm (dot-dashed line and *), 10.61 nm (upper solid line and ○), 11.67 nm (dashed line and ×), and 12.76 nm (lower solid line and +). Lines are from the present work, and symbols from Keenan *et al.* [8] and Kingston *et al.* [9]

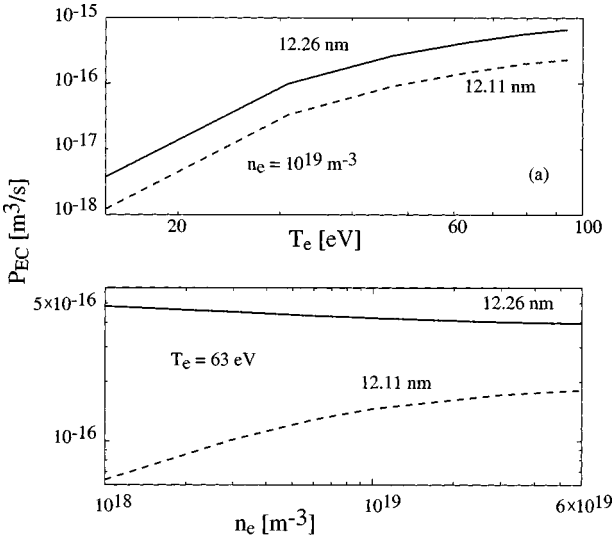

FIG. 5. Photon emission coefficients (P_{EC}, photons $\mathrm{m}^3\,\mathrm{s}^{-1}$) as functions of T_e (top, for $n_e=1\times10^{19}\,\mathrm{m}^{-3}$) and of n_e (bottom, for $T_e=63$ eV), for the following Ne VI lines: 12.26 nm (solid line), 12.11 nm (dashed line).

dipole velocity form of the transition operator matrix element [20]), and explicitly includes retardation effects [21]. RELAC's full multiconfiguration wave functions are used to compute the radiative transition rates; therefore, configuration mixing affects the calculated oscillator strengths. Comparisons with the dipole allowed A rates of Kingston *et al.* [9] show agreement to better than 5% for all transitions.

RELAC's wave functions are used in the quasirelativistic code CROSS [22] to compute collisional excitation cross sections between all the levels of a given ion in the DWA. CROSS is able to accomplish this by using the factorization theorem of Bar-Shalom, Klapisch, and Oreg, in conjunction with a semiempirical interpolation scheme [22] for the radial integrals required by the ''factored'' collision operator. The distorted-wave cross sections are then integrated over a Maxwellian distribution of free-electron energies to determine the final impact excitation rate coefficients. In particular, for Ne VII, comparison of the present collisional excitation rate coefficients for $2s2p\ ^3P-2s3d\ ^3D$ and $2s2p\ ^3P-2p3s\ ^3P$ with sophisticated R-matrix calculations by Ramsbottom *et al.* [23] show a consistent level of agreement to ±20%. Other $n=2-n=3$ excitations show a similar level of agreement. Comparisons with R-matrix calculations of collision strengths for $\Delta n=0$ $(n=2-n=2)$ electron-impact excitations [23–25] have shown agreement to better than ±5% for the $2s^2\ ^1S-2s2p\ ^1P$ transition, and a consistent 30–50% underestimate by CROSS of the $2s^2\ ^1S-2s2p\ ^3P$ transitions. These data are summarized in Table I. We have therefore adopted for the three Ne VII $2s^2\ ^1S-2s2p\ ^3P$ transitions the rates of Ramsbottom *et al.* [23]. Doing this, we find that the 11.67/10.61-nm and 12.76/10.61-nm line emission ratios of the present work are nearly identical with those of McKeown *et al.* [26], who calculated the ratios of these Ne VII lines using the complete set of R-matrix calculations of Ramsbottom *et al.* [23]. The 9.75/10.61-nm line emission ratio of the present work differs from theirs by +10% at an electron density of $10^{18}\,\mathrm{m}^{-3}$ and −5% at $10^{19}\,\mathrm{m}^{-3}$. This high level of agreement in relative line emissivities, and the excellent agreement between the simulations and data in Figs. 1 and 2, justify our choice of excitation rate coefficients for the Ne VII model.

The electron impact excitation rate coefficients and the radiative transition probabilities are then entered into the CR model. The relative populations for the levels of each ion at steady state are found by solving the coupled set of rate equations

$$n_j\left\{\sum_{i<j}^{M}(A_{j,i}+n_eQ^d_{j,i})+\sum_{k>j}^{M}n_eQ^e_{j,k}\right\}=\sum_{k>j}^{M}n_k(A_{k,j}+n_eQ^d_{k,j})+\sum_{i<j}^{M}n_in_eQ^e_{i,j}, \qquad (1)$$

where n_j is the relative population of level j, $Q_{j,i}$ is the collisional rate coefficient from level j to level i for excitation (e) or de-excitation (d), $A_{j,i}$ is the radiative transition probability from level j to level i, and M is the number of fine structure levels in the model for each ion. The configurations and the number of energy levels considered for each ion are listed in Tables II–IV. All electric and magnetic dipole and quadrupole radiative transitions ($E1$, $M1$, $E2$, and $M2$), as computed by RELAC, are taken into account. The resulting photon emission coefficient (P_{EC}) for a given transition is

$$P_{j,i}=\frac{n_j}{n_e}\sum A_{j,i}, \qquad (2)$$

where the sum over the A rates is over all multipoles connecting the two levels in question, and the electron density

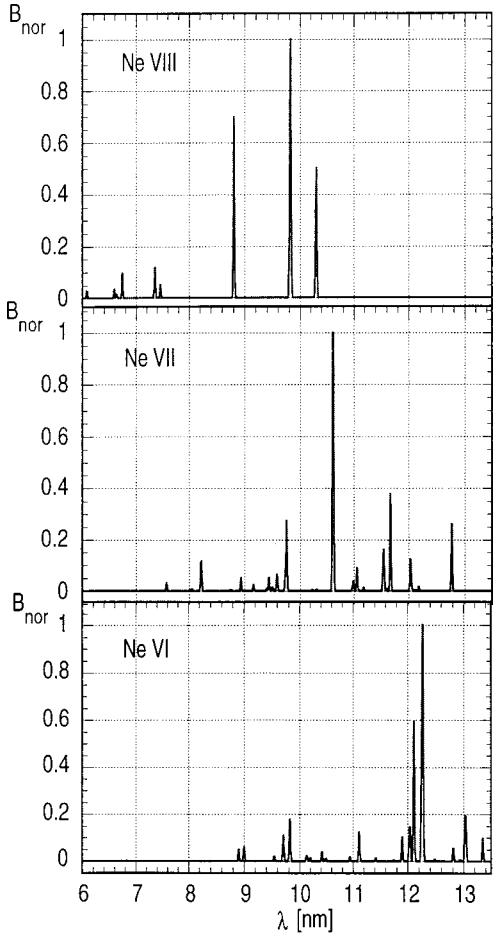

FIG. 6. The simulated spectrum of Fig. 1 (bottom) is decomposed in three spectra, each emitted by a single Ne ionization state. From top to bottom: Ne VIII, Ne VII, and Ne VI spectra.

n_e is divided out of the model. The resulting units are in photons $m^3\,sec^{-1}$. The CR level populations have been calculated at electron temperatures of 20%, 40%, 60%, 80%, 100%, and 120% of the first ionization potential for each charge state, and at six electron densities from $n_e=10^{18}$ to $6\times10^{19}\,m^{-3}$. Emission from B- and Be-like ions has also been computed at 5, 10, 30, and 50% of the ionization energy. The level populations found from Eq. (1) are normalized for each ion according to

$$\sum_{j=1}^{M} n_j = 1, \tag{3}$$

where the sum runs over all levels of a given ion. The calculated transition energies for EUV transitions of the present work can differ from experimental values by as much as 5% (RELAC is a relativistic code designed to calculate the structure of high-Z atoms [18,19]). The CR intensities for the transitions between two energy levels have been computed as described. To model the experimental spectra, measured transition energies have been used [27].

The lines detected in the 10-nm region are all due to $n=2-n=3$ transitions. The ''total'' P_{EC} summed over the fine structure components, are now presented and compared with previously reported values.

In Fig. 3, the P_{EC} of the Ne VIII $2s$-$3p$, $2p$-$3d$, and $2p$-$3s$ lines are given as functions of T_e, the wavelengths being, respectively, 8.81, 9.82, and 10.3 nm. They are increasing functions of T_e, as is always the case for $\Delta n=1$ transitions. Moreover, up to electron densities in the $10^{20}\,m^{-3}$ range, the P_{EC} are independent of n_e. Cochrane and McWhirter [28] have proposed formulas to evaluate the excitation rates Q_{exc} from the ground level to the $3s$, $3p$, and $3d$ levels. The fact that these P_{EC} are independent of n_e implies that, in the indicated n_e range, the $2p\ ^2P$ levels have negligible population and do not contribute to the $n=3$ level population. Since, moreover, cascades from higher levels are negligible, the Q_{exc} values of Cochrane and McWhirter [28] can be compared with the P_{EC} of our CR model, as shown in Fig. 3. The agreement is very good.

For Ne VII, $n=2$ and $n=3$ level populations are given by Lang [7] and Keenan *et al.* [8]. It is straightforward to get the P_{EC} of the lines emitted from the excited levels, since the transition probabilities are also given. In Fig. 4, the P_{EC} of the $n=2-n=3$ lines emitted by the $2s2p\ ^1P-2s3s\ ^1S$, $2s^2\ ^1S-2s3p\ ^1P$, $2s2p\ ^1P-2s3d\ ^1D$, and $2s2p\ ^3P-2s3d\ ^3D$ transitions are given as functions of T_e (top) for $n_e=3\times10^{19}\,m^{-3}$, and as functions of n_e (bottom) for $T_e=86$ eV. The corresponding wavelengths are, respectively, 12.76, 9.75, 11.67, and 10.61 nm. The curves of Fig. 4 at fixed n_e (top) are increasing functions of T_e, as is expected for $\Delta n=1$ transitions. On the other hand, Fig. 4 (bottom) shows an increasing behavior for the 10.61-nm triplet, whereas the other P_{EC} decrease with n_e. This is due to the well known effect of increasing population in the triplet levels and of decreasing population of singlet levels, as a consequence of electron collisions (the ground level, the only one populated at very low n_e, being singlet).

Lang *et al.* [10] have calculated the ratios of the three singlet-singlet lines to the 10.61-nm triplet-triplet lines as functions of n_e; these ratios show the existence of two n_e ranges. In the low-density range (corresponding to solar plasma densities) the ratios are of the order of 1–2 (for $T_e\sim50-200$ eV); they decrease to 0.2–0.3 in the high n_e range (practically independent of T_e). The θ-pinch measurements of Lang [7] fall in this n_e range. The transition region is between 10^{17} and $10^{19}\,m^{-3}$. Consequently, the curves of Fig. 4 correspond to the upper half of the transition region. Lang [7] and Lang *et al.* [10] have used the CR model of Keenan *et al.* [8] and Kingston *et al.* [9]; the plotted points in Fig. 4 are taken from these calculations. The agreement for the 10.61-, 11.67-, and 12.76-nm lines is quite good, the values from our model being generally higher by a factor between 1 and 1.5. On the other hand, for the 9.75-nm line the disagreement is clearly larger (the differences being of the order of 2). This point has been discussed by Lang *et al.* [10], who concluded that their P_{EC} values should be increased by a factor of 1.9 to get satisfactory 97.5/10.31 line intensity ratios, both in solar and θ-pinch plasmas. As stated above, our calculated line intensity ratios also show excellent agreement with those in the recent work by McKeown *et al.* [26].

In Fig. 5, for Ne VI, the P_{EC} values of the two strongest lines in the 10-nm range are plotted: the 12.26-nm line ($2s^22p\ ^2P-2s^23d\ ^2D$ transition) and the 12.11-nm line ($2s2p^2\ ^4P-2s2p3d\ ^4D$ transition). A transfer of population between systems of different multiplicity also appears in this

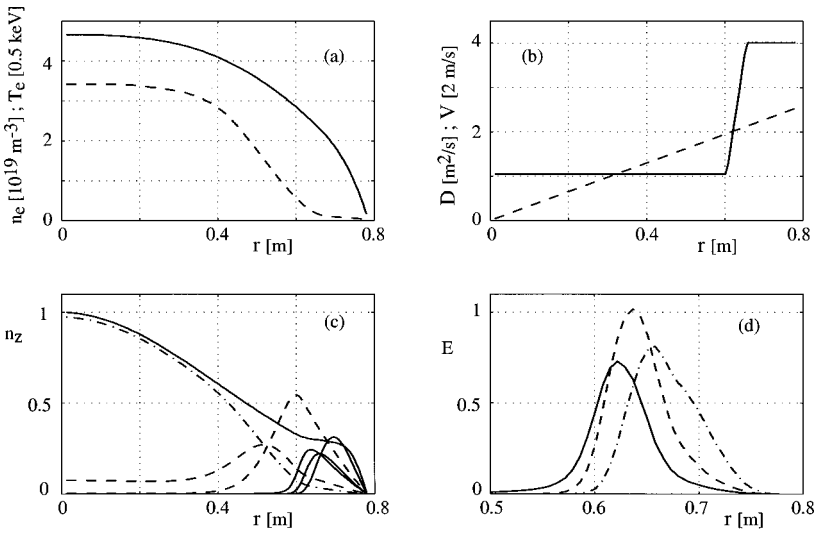

FIG. 7. Transport simulation for TS ergodic divertor plasmas. Radial profiles of (a) n_e (solid line) and T_e (dashed line), obtained by fitting the experimental data; (b) diffusion coefficient D and inward convection velocity V (solid and dashed line, respectively); (c) Ne ion densities n_z, normalized to the total Ne-ion density (solid line); charge states from Ne^{5+} to Ne^{10+} are shown [Ne^{10+} dot-dashed line, Ne^{8+}–Ne^{9+} (*3) dashed lines, Ne^{5+}–Ne^{7+} (*6) solid lines]; (d) emissivities E of the three Ne VIII, Ne VII, and Ne VI ''reference'' lines at 9.82, 10.61, and 12.26 nm (respectively, solid, dashed, and dot-dashed line), normalized to the largest peak emissivity.

figure. For the B-like sequence the ground state is doublet, and the quartet system levels are progressively populated with increasing n_e. It is for this reason that in Fig. 5 (bottom) the 12.11/12.26 line intensity ratio decreases with increasing n_e, both P_{EC} increasing with T_e, since both transitions are $\Delta n=1$; in solar plasma line intensity ratio analysis (e.g., Keenan *et al.* [11,29]), only $n=2-n=2$ line ratios have been considered.

IV. IMPURITY MODELING

The one-dimensional (1D) impurity transport simulation codes, used to simulate the TS and RFX experiments, are similar, differing only slightly in the numerical treatment. Both describe, for a given atomic species, in cylindrical geometry, ionization, recombination, and radial transport of the ions of charge z and density n_z [30].

For neon, the electron-induced ionization rate coefficients are taken from the Queen's University of Belfast assessment [31]. Radiative recombination is treated using the H-like approximation, modified to take into account that the valence shell can be partially occupied [32]. As far as dielectronic recombination is concerned, the treatment by Sobelman, Vainshtein, and Yukov is followed [33]. The corresponding data for the intrinsic impurities (carbon and oxygen) have been discussed by Carraro *et al.* [30]

The impurity flux density Γ_z is expressed as the sum of both diffusive and inward convective terms

$$\Gamma_z(r)=-D(r)\nabla n_z(r)-V(r)n_z(r), \tag{4}$$

where $D(r)$ and $V(r)$ are the radially dependent diffusion coefficient and inward convection velocity, respectively, both taken independent of the charge z of the ions. For the special case of a radially constant D, taking $V(r)=(r/a)\,V_A$ (a being the last mesh radius) yields at steady state a Gaussian profile for the total impurity density, $n_t(r)=n_t(0)\exp(-Sr^2/a^2)$, with a peaking parameter $S=aV_A/2D$. Experimental electron density, $n_e(r)$, and temperature, $T_e(r)$, profiles are used to evaluate the required atomic physics rate coefficients. For both devices, the steady-state ion radial distribution is obtained for Ne, O, and C. The transport coefficients are assumed to be the same for the three elements, and their radial dependence is obtained, in each device, in order to simulate simultaneously both the Ne spectra and the available intrinsic impurity data (as done, e.g., by Carraro *et al.* [30]).

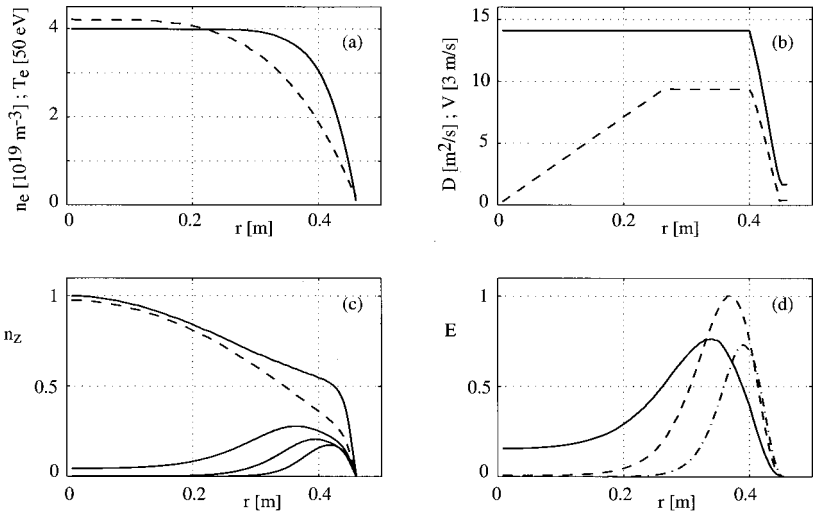

FIG. 8. Transport simulations for RFX plasmas. Radial profiles of: (a) n_e (solid line) and T_e (dashed line), obtained by fitting the experimental data; (b) diffusion coefficient D and inward convection velocity V (solid and dashed line, respectively); (c) Ne ion densities n_z, normalized to the total Ne ion density (solid line); charge states from Ne^{5+} to Ne^{8+} are shown [Ne^{8+} dashed line, Ne^{5+}–Ne^{7+} (*4) solid lines]; (d) emissivities E of the three Ne VIII, Ne VII, and Ne VI ''reference'' lines at 9.82, 10.61, and 12.26 nm (respectively, solid, dashed, and dot-dashed line), normalized to the largest peak emissivity.

V. SIMULATION OF THE NEON SPECTRA

The simulated spectra are shown in Figs. 1 (bottom) and 2 (bottom), for RFX and TS respectively. They have been obtained as discussed later in this section. In both cases the experimental and simulated spectra are normalized to the strongest line: the 9.82-nm Ne VIII line ($2p\ ^2P-3d\ ^2D$ transition) in Fig. 1, and the 10.61-nm Ne VII line ($2s2p\ ^3P-2s3d\ ^3D$ transition) in Fig. 2. In Fig. 6, the simulated spectrum of Fig. 1 has been decomposed, from top to bottom, in three partial spectra, including, respectively, only the Ne VIII, Ne VII, and Ne VI lines. For each sequence, normalization is to the strongest line: 9.82 nm for Ne VIII, 10.61 nm for Ne VII, and 12.26 nm for Ne VI ($2s^22p\ ^2P-2s^23d\ ^2$D transition).

The simulated Li-like Ne VIII spectrum seems satisfactory; in particular, the ratios of the three lines of Fig. 3 agree well with the observations. The simulated Be-like Ne VII spectrum also has satisfactory agreement with the observed features in Fig. 1. This level of agreement is only achieved when the DWA excitation rate coefficients for $2s^2\ ^1S-2s2p\ ^3P$ are ''updated'' with *R*-matrix data. The result of this update is to enhance the 10.61-nm ($2s2p\ ^3P-2s3d\ ^3D$ transitions) feature relative to the 11.67-nm ($2s2p\ ^1P-2s3d\ ^1D$) and the 9.75-nm ($2s^2\ ^1S-2s2p\ ^1P$) lines. For the B-like spectrum, the agreement between experiment and simulation can be considered satisfactory. It is worthwhile to underline that, in the TS spectrum of Fig. 2, the relative ratios of the strongest lines of the three isoelectronic sequences are different, but the comparison between experiment and simulation for the individual ionization states is still satisfactory.

Since the simulated spectra including all three Ne ionization states depend on the transport coefficients (because the ion charge distribution depends not only on the profiles of n_e and T_e, but also of the impurity transport coefficients), we shall now briefly present the details of the transport simulations for the two discharges discussed in this paper.

Previous simulations of impurity transport on TS with the ergodic divertor activated have shown the necessity to increase $D(r)$ (by a factor of 3 to 5, compared to Ohmic limiter discharges) in the peripheral ergodic layer, $V(r)$ being kept always linear. Figure 7 shows, for the TS plasma, radial profiles of the following: (a) n_e and T_e; (b) D and V; (c) a few Ne-ion densities (Ne^{5+} to Ne^{10+}), normalized to the total Ne ion density; and (d) the emissivities of the three ''reference'' lines (Ne VIII: 9.82 nm; Ne VII: 10.61 nm; Ne VI: 12.26 nm), normalized to the largest peak emissivity. It must be stressed here that the simulated Ne spectrum of Fig. 2 (bottom) is obtained assuming the same radial dependence of the transport parameters as in previous TS simulations, i.e., that required to satisfy the experimental H-like and He-like C ion line ratio values [30,34]. The peripheral $D(r)$ increase is ''adjusted'' to have the correct line intensity ratio of the three strong reference Ne lines. In the plasma core, the $D(r)$ and $V(r)$ profiles correspond to a peaking factor S of the order of 2.0, required, as explained in Sec. II, by the C and O experimental data analysis. From the analysis of laser blow-off injection experiments in TS [34,35], the existence of a reduced transport coefficient core region has been inferred. It has not been possible to take this into account in the present simulation, since the analyzed steady-state impurity distribution is essentially sensitive only to the peaking factor S. The visible bremsstrahlung and soft x-ray emissivities give the central impurity content, whereas the simulation of the C VI and C V line brightnesses gives the peripheral C content. The assumed diffusion coefficient is compatible with the Ne penetration time to the center at the beginning of the inflow.

Previous studies in RFX [12,13] have indicated that the diffusion coefficient $D(r)$ of both filling gas and impurities is a decreasing function of radius in the most external plasma region near the wall; this has been taken as a constraint in the RFX simulations. This radial dependence, which is opposite to that usually reported in tokamaks, is compatible with a transport mechanism based on parallel transport along stochastic magnetic field lines in the core region [13]. The $n_e(r)$ and $T_e(r)$ profiles [shown in Fig. 8(a)] are very flat, but the fact that the experimental C VI Lyα/C V R line-intensity ratio has a value of approximately 2 implies a peaking towards the center of the impurity profiles. Using only C-ion emission data, this ratio had been previously simulated (e.g., Carraro *et al.* [12]), taking D and V_A, respectively, in the range of 10–20 $m^2\,s^{-1}$ and of 100 $m\,s^{-1}$, with peaking factors S of the order of 1 to 2. As already mentioned, both D and V_A had been taken constant up to $r/a \cong 0.8$, and then decreased by about one order of magnitude around $r/a \cong 0.9$. In this way, the total ion density profile is a regularly decreasing function of radius.

The first simulations of the neon behavior in RFX with these transport assumptions did not agree with the spectrum in Fig. 1; the 10.61-nm Ne VI line was about one half as intense as the 9.82-nm Ne VIII line, i.e., as intense as the 10.3-nm Ne VIII line ($2p\ ^2P-3s\ ^2S$ transition). The only way to obtain a satisfactorily simulated spectrum has been to ''flatten'' the total Ne ion density profile in the outer plasma half. Since increased diffusion and/or reduced convection are required for this purpose, we have reduced $V(r)$ to a constant value of 30 m/s in the outer plasma half to obtain the simulated spectrum of Fig. 1 (bottom). The final $D(r)$ and $V(r)$ profiles are shown in Fig. 8(b). A C VI Lyα/CV R ratio of about 1.7 and a G ratio of 0.53, quite near the experimental values (taking into account errors on the line intensity ratio of the order of 10–20%) have been obtained. The Ne ion radial density profiles and the emissivities of the three Ne ''reference'' lines are shown, respectively, in Figs. 8(c) and 8(d).

VI. CONCLUSION

Neon injections have been performed in the reversed field pinch RFX and in the TS tokamak, with the purpose of producing peripheral radiative layers spreading uniformly the thermal load on the walls. Examples of experimental and simulated neon spectra in the 10-nm range are presented for both devices. These spectra include lines from Ne^{7+}, Ne^{6+}, and Ne^{5+} ions, i.e., lines emitted from neon ions of the Li-like, Be-like, and B-like isoelectronic sequences. CR models have been built for these three Ne ions, considering electron collisional excitation and radiative decay as populating processes of the excited states. The outcome of these calculations are photon emission coefficients for the lines emitted by the excited levels, for n_e and T_e values corresponding to the experimental conditions. Impurities are modeled with a 1D impurity transport code, calculating the steady-state ra-

dial distribution of the Ne ions. The Ne line brightnesses are evaluated in a post-process subroutine and simulated spectra are obtained. Three ionization states contribute to the experimental spectra, but it appears that the parts of the spectra corresponding to a single ionization state do not depend on the experimental conditions. The agreement between experimental and simulated single ionization spectra is good, thus giving confidence in the atomic data set. On the other hand, the superpositions of the three single ion spectra depend on the experimental conditions, as a consequence of the fact that the ion charge distribution depends not only on the n_e and T_e profiles, but also on the impurity transport coefficient profiles [namely, the diffusion coefficient $D(r)$ and the inward convection velocity $V(r)$] in the plasma region where the considered ionization states are emitting. As usual, the determination of the transport coefficients is not unique. For both devices an assumption on the radial dependence of one of these coefficients was necessary; this choice has been made on the basis of previous transport studies. On TS, the inward convection velocity $V(r)$ has been taken linear and $D(r)$ adjusted (increased) in the edge ergodic region to satisfy the experimental Ne data. On the other hand, on RFX, $D(r)$ was assumed to be radially constant, except in the most external plasma region near the walls, where $D(r)$ rapidly decreases. Subsequently, $V(r)$ has been adjusted (reduced in the outer plasma half) to satisfy the experimental Ne data. Outside the considered Ne emitting region, both coefficients are deduced by simulating intrinsic (carbon and oxygen) impurities.

On RFX, it has been concluded, from the simulation of the Ne spectrum in the 10-nm region, that the Ne density profile is almost flat for r/a values between 0.60 and 0.85. On the other hand, impurity peaking towards the center has been inferred from one of the C line intensity ratios. On TS, during the analyzed Ne injection, the ED was activated. An increased diffusion has been inferred in the peripheral ergodic layer, as previously deduced from C VI and C V line intensity ratio analysis [30,34].

ACKNOWLEDGMENT

A portion of this work was performed under the auspices of the U.S. Department of Energy by the Lawrence Livermore National Laboratory under Contract No. W-7405-Eng-48.

[1] P. E. Vandenplas, A. M. Messiaen, J. P. H. E. Ongena, U. Samm, and B. Unterberg, J. Plasma Phys. **59**, 587 (1998).
[2] L. K. Huang, S. Lippmann, B. C. Stratton, H. W. Moos, and M. Finkenthal, Phys. Rev. A **37**, 3927 (1988).
[3] D. J. Whyte, M. R. Wade, D. F. Finkenthal, K. H. Burrell, P. Monier-Garbet, B. W. Rice, D. P. Schissel, W. P. West, and R. D. Wood, Nucl. Fusion **38**, 387 (1998).
[4] R. Dux, A. Kallenbach, M. Bessenrodt-Weberpals, K. Behringer, H. S. Bosch, J. C. Fuchs, O. Gehre, F. Mast, W. Poschenrieder, H. Murmann, H. Salzmann, J. Schweinzer, W. Suttropp, the ASDEX-Upgrade Team, and the NI Team, Plasma Phys. Controlled Fusion **38**, 989 (1996).
[5] L. Lauro-Taroni, G. Corrigan, R. Simonini, J. Spence, E. Springmann, A. Taroni, P. Andrew, R. Giannella, P. J. Harbour, L. D. Horton, L. C. Ingesson, K. Lawson, C. F. Maggi, R. D. Monk, M. O'Mullane, and M. von Hellerman, Contrib. Plasma Phys. **38**, 242 (1998).
[6] L. Carraro, S. Costa, L. Marrelli, M. Mattioli, A. Murari, M. E. Puiatti, F. Sattin, P. Scarin, G. Telesca, M. Valisa, A. Canton, P. Franz, and R. Pasqualotto, in *Controlled Fusion Plasma Physics*, Proceedings of the 25th European Conference, Praha, 1998, edited by P. Paulo (European Physical Society, Geneva, 1998), Vol. 22C, p. 790.
[7] J. Lang, J. Phys. B **16**, 3907 (1983).
[8] F. P. Keenan, K. A. Berrington, P. G. Burke, A. E. Kingston, and P. L. Dufton, Mon. Not. R. Astron. Soc. **207**, 459 (1984).
[9] A. E. Kingston, P. L. Dufton, J. G. Doyle, and J. Lang, J. Phys. B **18**, 2561 (1985).
[10] J. Lang, P. L. Dufton, and A. E. Kingston, Solar Phys. **105**, 313 (1986).
[11] F. P. Keenan, E. S. Conlon, G. A. Warren, A. K. Pradhan, H. L. Zhang, D. H. Sampson, and K. G. Widing, Astrophys. J. **421**, 851 (1994).
[12] L. Carraro, M. E. Puiatti, F. Sattin, P. Scarin, M. Valisa, and M. Mattioli, Nucl. Fusion **36**, 1623 (1996).
[13] D. Gregoratto, L. Garzotti, P. Innocente, S. Martini, and A. Canton, Nucl. Fusion **38**, 1199 (1998).
[14] J. L. Schwob, A. W. Wouters, S. Suckewer, and M. Finkenthal, Rev. Sci. Instrum. **58**, 1601 (1987).
[15] A. Bar-Shalom and M. Klapisch, Comput. Phys. Commun. **50**, 375 (1988).
[16] M. Klapisch, Comput. Phys. Commun. **2**, 239 (1971).
[17] M. Aymar, M. Crance, and M. Klapisch, J. Phys. Suppl. **31**, C4-141 (1970).
[18] M. Klapisch, J. Schwob, B. Fraenkel, and J. Oreg, J. Opt. Soc. Am. **67**, 148 (1977).
[19] K. B. Fournier, At. Data Nucl. Data Tables **68**, 1 (1998).
[20] I. P. Grant, J. Phys. B **7**, 1458 (1974).
[21] E. Koenig, Physica (Amsterdam) **62**, 393 (1972), untranslated.
[22] A. Bar-Shalom, M. Klapisch, and J. Oreg, Phys. Rev. A **38**, 1773 (1988).
[23] C. A. Ramsbottom, K. A. Berrington, and K. L. Bell, At. Data Nucl. Data Tables **61**, 105 (1995).
[24] K. A. Berrington, P. G. Burke, P. L. Dufton, and A. E. Kingston, At. Data Nucl. Data Tables **26**, 1 (1981).
[25] K. A. Berrington, P. G. Burke, P. L. Dufton, and A. Kingston, At. Data Nucl. Data Tables **33**, 195 (1985).
[26] M. McKeown, F. P. Keenan, V. J. Foster-Woods, C. A. Ramsbottom, K. L. Bell, and R. H. G. Reid, J. Phys. B **31**, 4477 (1998).
[27] R. L. Kelly, J. Phys. Chem. Ref. Data Suppl. **16**, 1 (1987).
[28] D. M. Cochrane and R. W. P. McWhirter, Phys. Scr. **28**, 25 (1983).
[29] F. P. Keenan, V. J. Foster, R. H. G. Reid, J. G. Doyle, H. L. Zhang, and A. K. Pradhan, Astron. Astrophys. **300**, 534 (1995).
[30] L. Carraro, M. Mattioli, F. Sattin, C. DeMichelis, J. T. Hogan, W. Mandl, M. E. Puiatti, P. Scarin, and M. Valisa, Phys. Scr. **55**, 565 (1997).
[31] M. A. Lennon, K. L. Bell, H. B. Gilbody, J. G. Hughes, A. E.

Kingston, M. J. Murray, and F. J. Smith, J. Phys. Chem. Ref. Data **17**, 1285 (1988).

[32] M. Mattioli, Cadarache Laboratory Report No. EUR-CEA-FC 1346, 1988 (unpublished).

[33] I. I. Sobelman, L. A. Vainshtein, and E. A. Yukov, *Excitation of Atoms and Broadening of Spectral Lines* (Springer-Verlag, Berlin, 1981).

[34] M. Mattioli, C. DeMichelis, and P. Monier-Garbet, Nucl. Fusion **35**, 807 (1995).

[35] M. Mattioli, M. Erba, T. Dudok de Wit, A. L. Pecquet, J. L. Segui, and J. C. Vallet, Nucl. Fusion **38**, 189 (1998).